The International Journal of Advanced Manufacturing Technology (2025) 139:2393–2408
https://doi.org/10.1007/s00170-025-16030-8

ORIGINAL ARTICLE

Hot workability behaviour of AISI316 stainless steel: constitutive analysis, dynamic material modelling, and finite element simulation

Japheth Obiko[1] · Micheal Bodunrin[2] · Desmond Klenam[2] · Brendon Mxolisi[1] · Malatji Nicholus[1]

Received: 17 April 2025 / Accepted: 27 June 2025 / Published online: 5 July 2025
© The Author(s) 2025

Abstract

Most forged components undergo microstructural changes due to severe working conditions, which in turn affect product quality. In-depth understanding of hot deformation plays a key role in process parameter optimisation and improving final product quality. Therefore, this article reports the metal flow behaviour of AISI 316 steel. Uniaxial compression tests were conducted using Gleeble® 3500 thermal–mechanical equipment. The test conditions were 900–1050 °C and 0.1–15 s^{-1}. Constitutive models and processing maps were developed using experimental data. The constitutive model was used as input code for finite element simulation to validate the optimal processing window identified using processing maps. The results show that flow stress–strain curves exhibited dynamic recovery as a deformation mechanism. The flow stress increased with an increase in the strain rate or decrease in deformation temperature. The material parameter values were stress exponent n (7.87) and the activation energy Q (353.076 $kJmol^{-1}$). The statistical parameters analysis results were Pearson's coefficient R (0.995) and average absolute relative error (AARE) (2.53%). The statistical results show a good correlation between the predicted and experimental data. The developed constitutive model exhibited high accuracy in predicting the flow stress behaviour of the steel studied. The optimal processing window was 900/1050 °C and 15 s^{-1} as verified by finite element simulation. The study has shown that finite element simulation is an efficient and effective method of analysing industrial metal forming processes.

Keywords Constitutive equation · Processing maps · Finite element simulation · Stress exponent · Activation energy

1 Introduction

Stainless steel is popular for industrial applications, especially in nuclear power plants, defence, and marine industries [1]. This popularity is due to good strength, wear, and corrosion resistance [2–5]. These superior properties are due to the effect of alloying elements such as Cr, Ni, and Mo [6, 7]. These steels exhibit high-temperature strength and corrosion resistance during industrial service, especially in aerospace and power plants [8, 9]. Stainless steels fall under the following categories: austenitic, ferritic, martensitic, duplex, and precipitation hardening [6, 10]. For example, austenitic steels contain 12–25 wt% Cr, 8–25 wt% Ni, and 0–6 wt% Mo. These alloying elements improve mechanical properties at high in-service temperatures. This steel family comprises 304, 316, and 316L [11].

316L steel finds application as a structural material due to its high strength, oxidation resistance, and superior toughness [8, 12, 13]. During production, 316L components undergo a complex deformation process to improve the mechanical properties and refine the microstructure of the final product [14, 15]. Therefore, controlling the final microstructure for enhanced mechanical properties of the steel is paramount. Thus, during the processing route, there is a need to control the hot working process and optimise the process parameters to ensure a high-quality product. To this end, 316L steel has been widely studied and reported in the literature [12, 16]. However, there is still scanty information on process optimisation and an in-depth understanding of metal flow behaviour as affected by different loading conditions. Therefore, the relationship between the flow behaviour and the process parameters needs an exhaustive study.

✉ Japheth Obiko
japheth.obiko97@gmail.com

[1] Department of Chemical, Metallurgical and Material Engineering, Tshwane University of Technology, Pretoria, South Africa

[2] School of Chemical, Metallurgical Engineering, University of Witwatersrand, Johannesburg, South Africa

Understanding metal flow behaviour during deformation is of great concern to engineers and designers. The material undergoes large deformation during forming, causing complex deformation mechanisms and making analysis difficult [17]. Constitutive equations accurately analyse metal flow patterns during forming. These equations investigate the relationship between flow behaviour and process parameters. This analysis provides an accurate prediction of the flow stress behaviour of a material under a given loading condition [18]. Therefore, the accuracy of the constitutive equations is paramount. These equations act as input in the finite element method (FEM) simulation codes for studying the forming process. Finite element simulation reduces production costs and time. Moreover, FEM tools assist in developing new metal forming techniques and process parameters optimisation of the existing ones, such as the Mannesmann industrial process used for the production of seamless tubes.

Additionally, processing maps based on dynamic material modelling (DMM) provide a means of studying hot deformation and process parameter optimisation [19–21]. This technique identifies the safe and unsafe deformation regimes during forming. Hence, this model identifies the processing window for the deformation process for a given loading condition (strain, strain rate, and temperature) [22, 23]. Then, the question is why model metal forming processes now and then? These models provide insights into metal flow patterns and microstructure evolution associated with deformation mechanisms during forming [24]. The deformation mechanism also depends on the chemistry and the loading conditions during deformation [25]. Therefore, the accuracy of metal-forming analysis improves production costs and time, enhancing the production of high-quality products. The application of processing maps and constitutive equations in analysing the deformation process is readily available in the literature [26, 27]. However, the relationship between the processing maps and finite element simulation models in analysing the deformation process is conspicuously missing. This study aimed to develop the constitutive equations using the flow stress–strain data obtained from Gleeble® thermal–mechanical equipment to predict the flow stress behaviour of 316L steel. The constitutive equations are input computer codes for the finite element simulation modelling. The model then simulates the metal forming process in the optimal processing window obtained using processing maps. The use of FEM simulation was to verify the accuracy of the processing maps.

2 Experimental procedure

Table 1 shows the chemical compositions of austenitic 316 stainless steel used in this study. Figure 1 shows the initial microstructure of the steel studied. The microstructure exhibited a fine equiaxed and martensitic structure. The average grain diameter of about 13.8 µm was measured using ImageJ software. Sample geometry of 8 mm Ø and 12 mm length was sectioned from the metal rod supplied by Kensmetal Industries. A uniaxial hot compression test was conducted using the Gleeble® 3500 thermal–mechanical equipment. The test parameters used in this study were a forming temperature of 900–1000 °C and a strain rate of 0.1–15 s^{-1}. The deformation process was done under vacuum. K-type thermocouples were welded at the sample midspan to measure and control the deformation temperature against the preset temperature during testing. Nickel and graphite pastes assisted in limiting interfacial friction between the workpiece and ISO-T anvil. Figure 2 shows the thermal history during forming. The test samples were heated to 1100 °C (austenitisation temperature) at a heating rate of 5 °C/s and held for 180 s. This procedure ensures that microstructure homogenisation occurs. After austenitisation, the samples were cooled at a rate of 10 °C/s to the deformation temperature and soaked for 60 s. In this stage, the reduction of the thermal gradient within the sample occurs before deformation. All test samples were deformed to a true strain of 0.7, then rapidly air-cooled to room temperature, as shown in Table 2.

Fig. 1 Optical micrographs of as-received steel

Table 1 Chemical composition of AISI316 stainless steels (in wt%)

C	Mn	Si	Cr	Mo	Ni	P	N	S
0.025	1.41	0.41	16.16	2.00	10.22	0.025	0.043	0.025

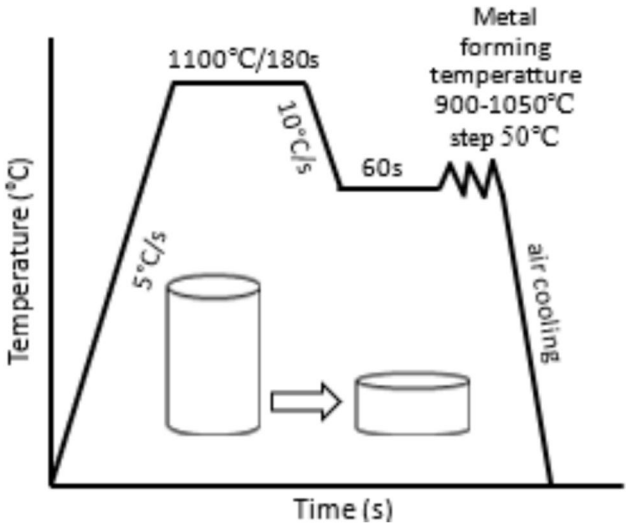

Fig. 2 The thermal profile during deformation

Table 2 Hot compression test parameters

Strain rate $\dot{\varepsilon}$ (s^{-1})	0.1	1	10	15
Temperature (°C)	900	950	1000	1050

3 Results and discussion

3.1 Flow stress–strain curves

Figure 3 shows the experimental stress–strain curves of hot forming tests for austenitic stainless steel at different forming conditions. In the study of the flow stress–strain curves, the following were observations:

- The flow curves show that flow stress is sensitive to the deformation conditions (temperature, strain rate and strain). At a constant forming temperature, an increase in the deformation temperature caused a decrease in flow stress, and vice versa. Similarly, for a given strain rate, the flow stress increased with an increase in the deformation temperature decreased.
- The flow curve exhibited two main deformation stages: work-hardening (WH) and dynamic softening. The characteristic point in the flow curves indicates the start and end of these two deformation mechanisms. For example, at strain ~ 0.2, the flow stress increased rapidly. This phenomenon can be attributed to work-hardening due to the high generation rate of density dislocation [28]. After the 0.2 strain, a balance between work-hardening and dynamic softening occurs, mainly dynamic recovery (DRV) for the steel studied. At this stage, the flow stress attains a steady-state condition. At this stage, WH + DRV reaches a state of equilibrium, causing a constant dislocation density. The flow curves indicate that DRV was the dominant softening mechanism. At a strain rate of 0.1, the flow stress curves exhibited an alternating WH + DRV. This phenomenon may be due to the effect of interfacial friction.
- The deformation mechanisms that occur during forming control the microstructure evolution. The microstructure formation dictates the flow stress behaviour [29]. However, these deformation mechanisms are affected by deformation conditions. Therefore, there is a need to optimise the loading conditions.
- The studied steel exhibited DRV as the softening mechanism. This steel has high stacking fault energy, thus exhibiting DRV behaviour. This behaviour means the studied steel readily re-arranges into a polygonal structure through climb and cross slip dislocation during deformation.

3.2 Constitutive analysis

Constitutive equations provide an efficient method to study the flow stress behaviour of metals and alloys during deformation. For example, Arrhenius-type equations find more application due to their simplicity in describing the deformation behaviour. This equation is as follows:

$$\dot{\varepsilon} = Af(\sigma)exp\left(\frac{-Q}{RT}\right) \tag{1}$$

where $f(\sigma) = \sigma^{n'}$ is used in low flow stress region ($\alpha\sigma < 0.8$), $f(\sigma) = exp(\beta'\sigma)$ applied in high flow stress ($\alpha\,\sigma > 1.2$), and $f(\sigma) = [\sin h(\alpha\sigma)]^n$ used for a wide range of flow stress. The unknown terms in Eq. (1) are defined as: $\dot{\varepsilon}$ (strain rate in s^{-1}), T(deformation temperature in Kelvin K), and Q (the activation energy of the material during deformation in kJ.mol−1. The stress value (peak stress σ_p, saturation flow stress σ_{sat}, and steady-state stress σ_{ss}) in the stress function $f_{(\sigma)}$, is obtained directly from the experimental flow stress–strain curves. The n (stress exponent), n', β, and α are material constants and $\alpha \approx \beta'/n'$ [30].

Sellars and Tegart [31] developed the constitutive Eq. 2. This equation characterises the metal flow behaviour for most engineering materials. This equation has been widely used and universally accepted by experts in this field [32–34].

$$\dot{\varepsilon} = A[\sin h(\alpha\sigma)]^n\, exp\left(\frac{-Q}{RT}\right) \tag{2}$$

The unknown values in Eq. 2 are A, α, and n are material constants, σ is the flow stress (MPa) directly obtained from the stress–strain flow curves, Q is the activation

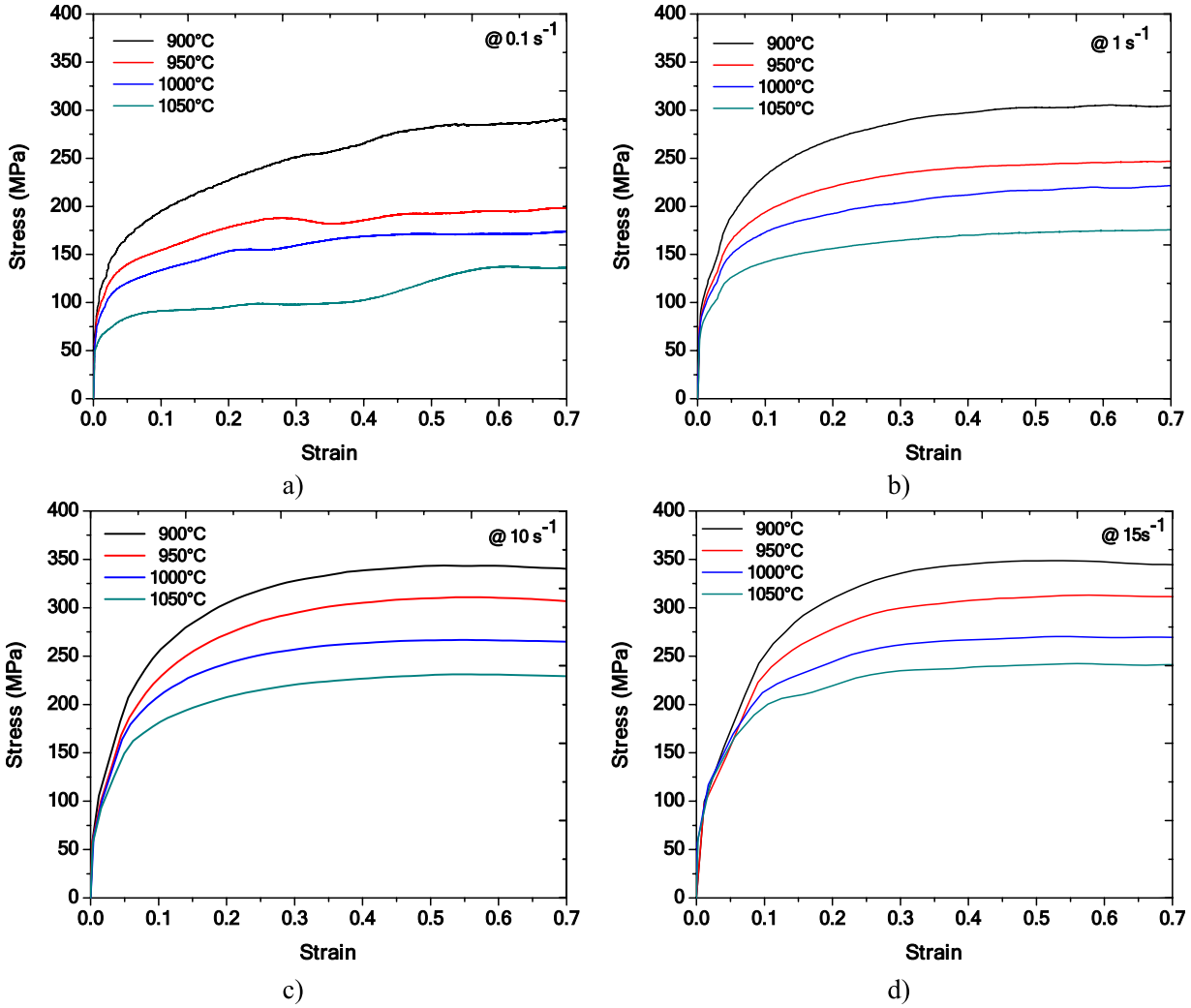

Fig. 3 The flow stress–strain curves (the colour code indicated loading at different deformation temperature)

energy, R is the gas constant, and T is the deformation temperature (in Kelvin). This equation (Eq. 2) can be applied to analyse flow stress behaviour at all stress levels. The material constants and activation energy are calculated using the peak/steady state stress directly obtained from the flow curves [16]. However, materials with high stacking fault energy do not exhibit a peak stress. The flow stress–strain of these materials exhibits dynamic recovery as the softening mechanism. Hence, the flow stress reaches a steady-state value. For this case, saturation flow stress, as suggested by Laasraoui and Jonas [35], is used to determine the material constants.

In this study, the flow stress–strain curves exhibited dynamic recovery behaviour. Therefore, the material constants and activation energy were analysed using saturation flow stress (σ_{ss}) obtained directly from the flow stress curves. Then, Eq. 2 can now be written as follows:

$$\dot{\varepsilon} = A\left[sinh(\alpha\sigma_{ss})\right]^{n} exp\left(\frac{-Q}{RT}\right) \tag{3}$$

3.3 Determination of material constants

Using Figs. 4 and 5, the material constants can be calculated as follows.

The stress multiplier α is obtained by determining the value of n' and β. Solving the power law (Eq. 4) for low flow stress and the exponential law (Eq. 5) for high stresses at constant temperature by taking the average of the slope of the curves.

$$\text{At low flow stress}: \; n' = \frac{\partial In\dot{\varepsilon}}{\partial In\sigma_{ss}} \tag{4}$$

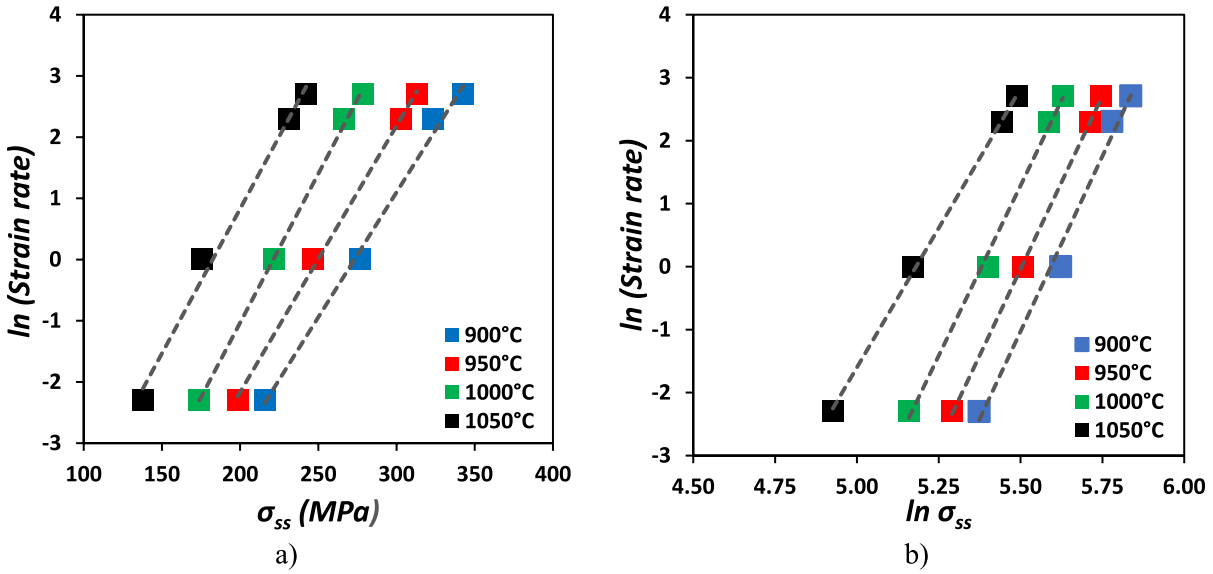

Fig. 4 Graphs of **a** *ln* strain rate vs. σ_{ss} to determine β and **b** *ln* strain rate vs. *ln* (σ) to determine n'

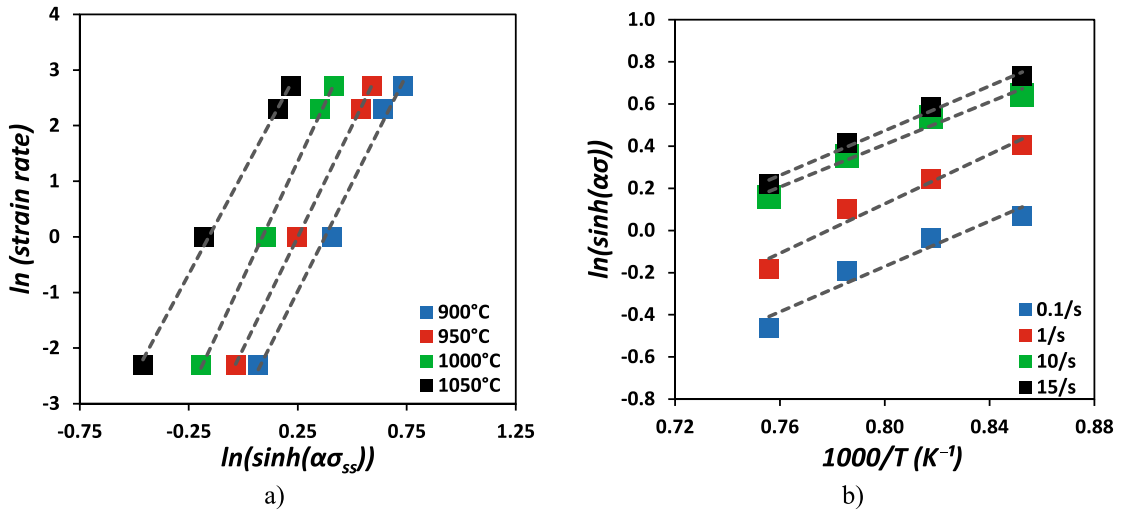

Fig. 5 Graphs of **a** *ln* strain rate vs. *ln* (sin*h* ($\alpha\sigma_{ss}$)) to determine n and **b** *ln* (sin*h* ($\alpha\sigma_{ss}$)) vs. 1000/T (K^{-1}) to determine the activation energy Q

$$\text{At high low stress}: \ \beta = \frac{\partial In\dot{\varepsilon}}{\partial \sigma_{ss}} \tag{5}$$

$$Then: \ \alpha = \frac{\beta}{n'} \tag{6}$$

At constant temperature, from Eq. 3, solve and take its partial derivative with ln $\dot{\varepsilon}$:

$$\frac{1}{n} = \frac{\partial ln\left[sinh(\alpha\sigma_{ss})\right]}{\partial ln\dot{\varepsilon}} \tag{7}$$

Also, at constant strain rate $\dot{\varepsilon}$:

$$Q = kn\frac{\partial ln\left[sinh(\alpha\sigma_{ss})\right]}{\partial \frac{1}{T}} \tag{8}$$

To fully characterise the contribution of strain rate and forming temperature, the Zener–Holloman parameter (Z) provides information on flow behaviour. The Zener–Holloman parameter equation is given as shown in Eq. 9. Solving Eq. 9 gives Eq. 10. Equation 10 is used to determine the value of *lnA* from Fig. 6.

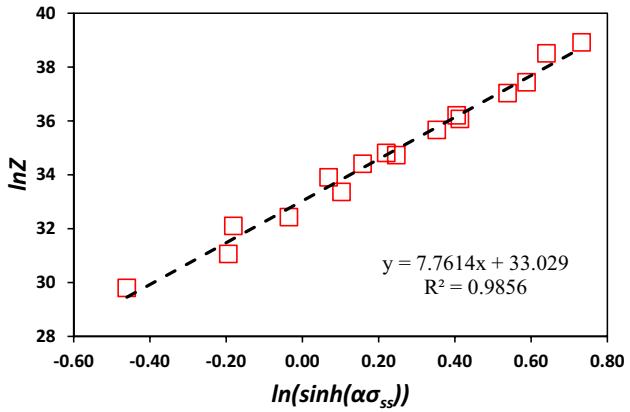

Fig. 6 Linear relationship between *ln Z* and *ln* (sin*h* ($\alpha\sigma_{ss}$))

Table 3 Material constants obtained from the constitutive equations

	Material constants				
β	0.0473	0.0435	0.0487	0.0408	0.0451
n'	10.801	8.8513	11.124	10.993	10.4423
α					0.0043
n	7.3066	8.0195	8.367	7.7962	7.8723
k	5.2971	5.0412	5.8629	5.377	5.3946
R					8.314
Q					353.0760
lnA					33.029
A					2.2096×10^{14}

$$Z = \dot{\varepsilon}\ exp\left[\frac{Q}{RT}\right] = f(\sigma) = A\left[sinh\left(\alpha\sigma_{ss}\right)\right]^{n} \tag{9}$$

Taking the natural logarithm on both sides of Eq. 9:

$$InZ = InA + n\ In\ sinh(\alpha\sigma_{ss}) \tag{10}$$

Therefore, the flow stress σ_{ss} can be expressed as follows:

$$\sigma = \frac{1}{\alpha} In\left\{\left(\frac{Z}{A}\right)^{1/n} + \left[\left(\frac{Z}{A}\right)^{2/n} + 1\right]^{1/2}\right\} \tag{11}$$

By substituting the material constants and activation energy values, as given in Table 3, into the hyperbolic sine law in Eq. 3, the study developed a constitutive equation for the steel studied (Eq. 12). The equation for predicting the flow stress behaviour of the studied steel is as follows:

$$\dot{\varepsilon} = 2.2096 \times 10^{14} sinh(0.0043\sigma_{ss})^{7.87} exp\left[\frac{-353076}{RT}\right] \tag{12}$$

From Eq. 13, the saturation flow stress under different conditions for the steel investigated can be determined as follows:

$$\sigma_{ss} = \frac{1}{0.0043} In\left[\left(\frac{Z}{2.2096 \times 10^{14}}\right)^{\frac{1}{8}} + \left(\left(\frac{Z}{2.2096 \times 10^{14}}\right)^{\frac{2}{7.87}} + 1\right)^{\frac{1}{2}}\right] \tag{13}$$

where $Z = \dot{\varepsilon}\left[\frac{353076}{RT}\right] = 2.2096 \times 10^{14}\left(sinh(0.0043\sigma_{ss}\right)^{7.87}$

The *Z*-parameter is obtained by substituting the activation energy in Eq. 13. The *Z*-value shows the combined effect of strain rate and forming temperature during forming. Figure 6 shows the linear correlation between *lnZ* and *ln* (sin*h* ($\alpha\sigma_{ss}$)). The correlation coefficient (R^2) was 0.9856. This value (R^2) shows that *ln* Z had a good linear relationship with *ln* (sin*h* ($\alpha\sigma_{ss}$)). The intercept of the *lnZ* -*ln* (sin*h* ($\alpha\sigma_{ss}$)) plot gave the *ln* A value of 33.029. Thus, the shape factor A was 2.2096×10^{14}. The material parameters are in Table 3.

Using the equation suggested by Sellars and Tergat [1], the activation energy *Q* and stress exponent were obtained using experimental flow stress–strain data. The *Q*-value was within the acceptable range. This value only indicates the deformation difficulty. In this study, the stress exponent *n*-value is 7.87. The *n*-values are generally affected by the chemical composition of the material and forming parameters. For example, at higher strain rates and lower deformation temperatures, higher *n*-values are expected [2]. The higher *n*-value is due to precipitates present during deformation, causing the interaction between the precipitates and dislocation movement [36, 37]. This interaction impedes metal flow during deformation [3]. Therefore, it is imperative to ensure that deformation operations are done in the austenite phase after dissolution of carbides. In this phase, the material deforms easily, hence reducing defect formation. To this end, the study observes that the *n*-value is sensitive to the deformation temperature. Therefore, there is a need to determine the optimal deformation temperature. The stress exponent value obtained in the study was within the range reported in the literature [12, 16].

Similarly, the activation energy *Q* was 353.076 kJ mol^{-1}. This *Q*-value was within the range of those reported in the literature [2, 16, 38]. The *Q*-value obtained in this study was higher than the diffusion activation energy of iron in austenite 270 kJ mol^{-1} [4] and alpha ferrite 250 kJ mol^{-1} [5]. The alloying elements in these steels caused variations in *Q*-value [6]. However, the calculated *Q*-values serve as an indicator of the resistance to deformation during forming.

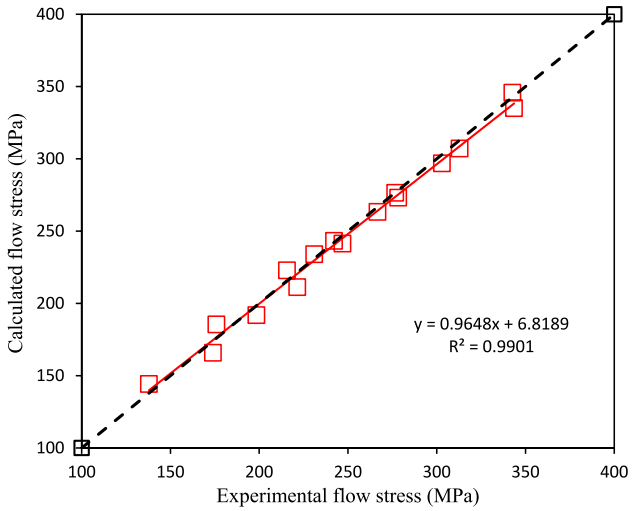

Fig. 7 Relationship between predicted and experimental flow stress

3.4 Model verification

The developed model (Eq. 12) was verified by comparing the predicted and experimental flow stress data. Figure 7 shows the linear relationship between the predicted and experimental flow stress data for all conditions tested. The correlation coefficient R^2 was 0.994, showing a close correlation of the two parameters (predicted and experimental data). Further analysis of the developed model, the study used statistical parameters: Pearson's coefficient R (Eq. 18) and the average absolute relative error (AARE) (Eq. 19). These parameters assist in evaluating the validity of the developed equation in predicting the flow stress behaviour [26, 27, 39].

$$R = \frac{\sum_{i=1}^{N}\left(M_i - \overline{M}\right)\left(P_i - \overline{P}\right)}{\sqrt{\sum_{i=1}^{N}\left(M_i - \overline{M}\right)^2 \sum_{i=1}^{N}\left(P_i - \overline{P}\right)^2}} \tag{14}$$

$$AARE(\%) = \frac{1}{N}\sum_{i=1}^{N}\left[\frac{M_i - P_i}{M_i}\right] \tag{15}$$

In Eqs. 14 and 15, the unknown parameters are as follows: M is the experimental flow stress, P is the predicted saturation flow stress, $\overline{M}$ is the average values of M, and $\overline{P}$ is the average values of P.

From the analysis, the following results were obtained:

- The Pearson's coefficient (R) for studied steel was 0.995. This value shows a good relationship between predicted and experimental data, where 1.0 usually indicates a perfect correlation.
- The AARE analysis usually gives a better accuracy for the parameters studied. The high AARE accuracy is due to this parameter considering the relative error of each flow stress term. The lower value of AARE indicates a higher accuracy of the developed constitutive model in predicting flow stress.
- The percentage error in this study was 2.53%. This value indicates a higher accuracy of the model in predicting the flow stress behaviour of the steel studied.
- The study concluded that the developed model had high statistical accuracy in predicting the flow stress behaviour of austenitic stainless steel for all test conditions. Hence, the study recommends the developed model for analysing any industrial metal forming process in the manufacturing supply chain.

4 Dynamic material modelling

The main objective of the forming process is to determine constitutive parameters. These parameters are used to develop the mathematical equation for predicting the flow stress behaviour during forming. However, the quality of the final product largely depends on the determination of the optimal processing window during deformation. Prasad et al. [40] developed dynamic material modelling (DMM) techniques for analysing metal forming behaviour. This technique has become an integral part of studying and optimising metal-forming processes. This technique uses processing maps to determine the optimal processing window during hot forming. These maps identify the 'safe' and 'unsafe' regions for metal processing scheduling. The processing maps are constructed by superimposing the instability map on the power dissipation map [41]. During forming, the material stores energy. An increase in temperature and strain rates causes an increase in power dissipation. The power dissipation efficiency is as [39, 42]:

$$\eta = \frac{2m}{m+1} \tag{16}$$

The parameter η in Eq. 16 indicates the mechanism responsible for the microstructure change. Hence, it shows the proportion of the power dissipated as the deformation causes microstructural change. The m-value in Eq. 16 is the strain rate sensitivity obtained from the polynomial equation of $ln\,\sigma$ against the $ln\dot{\varepsilon}$ graph. The strain sensitivity equation is in Eq. 17 [41, 43]:

$$m = \frac{\partial ln\sigma}{\partial ln\dot{\varepsilon}} \tag{17}$$

The m-values mainly depend on the loading conditions. This value ranges between 0 and 1 for stable (safe)

deformation regions, and negative values suggest unsafe deformation conditions. However, several instability equations have been developed. For example, Murty, Rao, and Kashyap [44] reviewed some instability equations. The study recommended the Murty instability criterion for stable materials with non-constant m-value as in Eq. 18 [45]:

$$2m < \eta \tag{18}$$

Solving the inequality gives:

$$\xi(\dot{\varepsilon}) = \frac{2m}{\eta} - 1 < 0 \tag{19}$$

The $\xi(\dot{\varepsilon})$ values in Eq. 19 are obtained using a cubic spline function for all deformation conditions. The instability map is developed on the temperature and strain rate space. Instability regions have a negative $\xi(\dot{\varepsilon})$ value. This region indicates the metal flow instability behaviour associated with flow localisation wedge cracking and adiabatic shear band. This study used Eq. 16 to develop a power dissipation map and Eq. 19 for instability maps for the steel studied.

Figure 8 shows the power dissipation and instability maps for the steel studied. The maps had no marked difference between the dissipation efficiency and instability maps. Therefore, the contour maps in this study are the processing maps. The contour lines (Fig. 8a) indicate the power dissipation efficiency η calculated using Eq. 16 and the flow instability $\xi(\dot{\varepsilon})$ value (Fig. 8c). The highest η-value was 34%, which occurred at loading conditions: temperature of 900 °C and strain rate of

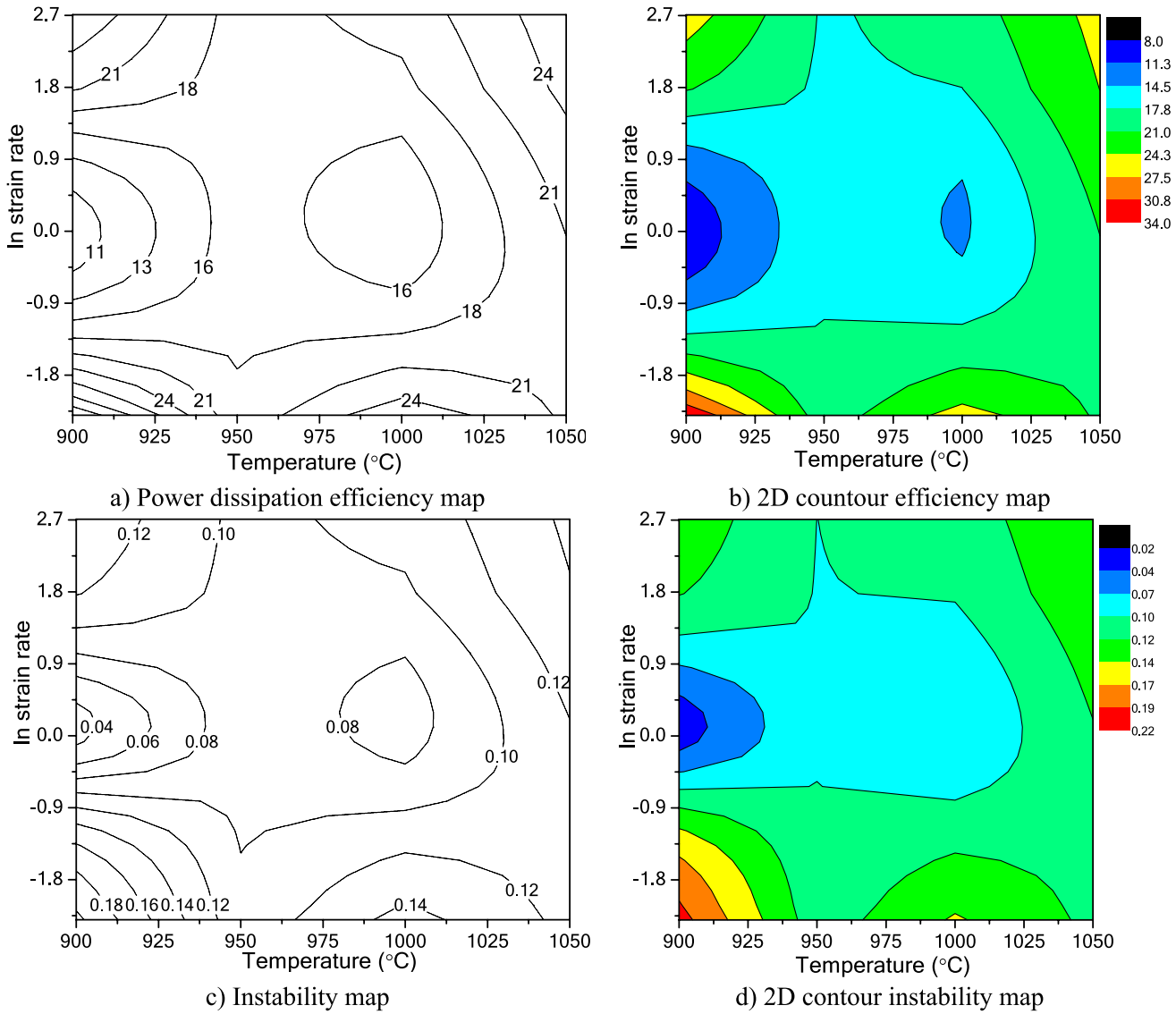

Fig. 8 Plots of processing maps for SS316 steel (the colour codes indicate different deformation regions)

0.1 s^{-1}. The peak efficiency range was 34–24%. These peak efficiencies occur in three regions. The first region lies between the temperature range of 900–925 °C and strain rate of 0.1 s^{-1}, with efficiency of 34–27%. The second region was at a temperature of 1000 °C and strain rate of 0.1 s^{-1}, with efficiency of 24%. The third region was at temperatures of 900 °C and 1050 °C and a strain rate of 15 s^{-1}, with a η-value of 24%. The lowest η-values were 11–16% at 900–925 °C and 1000 °C deformation temperatures and 1 s^{-1} strain rate. A lower η-value means that low energy caused microstructure changes during deformation. Regions with lower η-value are undesirable for the deformation of this steel. The instability map shows that this region had $\xi(\dot{\varepsilon})$ value of 0.04–0.08. Hence, in this region, the material exhibited low ductility. Therefore, deformation in regimes with low and η-value will cause brittle fracture. These areas are undesirable for the secondary processing of critical structural and functional components for engineering applications. The study recommends an optimal processing window of 900–925 °C at a strain rate of 0.1 s^{-1} for the steel studied.

5 Numerical simulation

Researchers have extensively studied metal flow behaviour for metals and alloys using the finite element method FEM [46–49]. This technique provides a reliable approach to predicting the behaviour of a physical phenomenon. In the past, most manufacturing industries were largely dependent on the experience of engineers and designers [50]. This approach was costly and time-consuming [51]. With the introduction of high-processing computers, simulation software has become handy in optimising process parameters and analysing manufacturing processes. For example, the DEFORM®3D FEM simulation code has applications in studying metal flow behaviour, such as stress and strain distribution during forming [48, 49, 52]. In metal forming, FEM simulation codes are based on experimental data analysed using constitutive equations. Therefore, this study used DEFORM®3D software version 11 to study the effect of loading conditions (optimal conditions obtained processing maps) on the metal flow behaviour. The study developed a material database that mimics the actual material used in this study. The constitutive equations form the input codes. The physical properties of the steel were determined using JMatPro software.

Table 4 shows the material parameters for AISI316 steel. Figure 9 shows the development of the material database in the software input window. The FEM simulation analysis uses a rigid viscoplastic formulation [48, 53]. The computation equations governing the metal-forming process are widely covered in the literature [54]. The die and test sample geometry were modelled using the in-built primitive modeller in the software. The simulation sample geometry was similar to a physical sample used in the Gleeble® physical simulation equipment. Table 5 provides the numerical simulation parameters and conditions. The deformation of the test sample was from 15 to 6.3 mm, $\varepsilon \approx 0.64$.

5.1 Deformation process

Deformed test samples undergo inhomogeneous deformation due to the interfacial friction between the die and the workpiece. The formed sample exhibits three deformation

Table 4 Constitutive parameters for AISI316 steel

AISI316L steel	α	β	n'	n	Q (Jmol^{-1})	A
Value	0.0043	0.0451	10.4423	7.87	353,076	2.2096×10^{14}

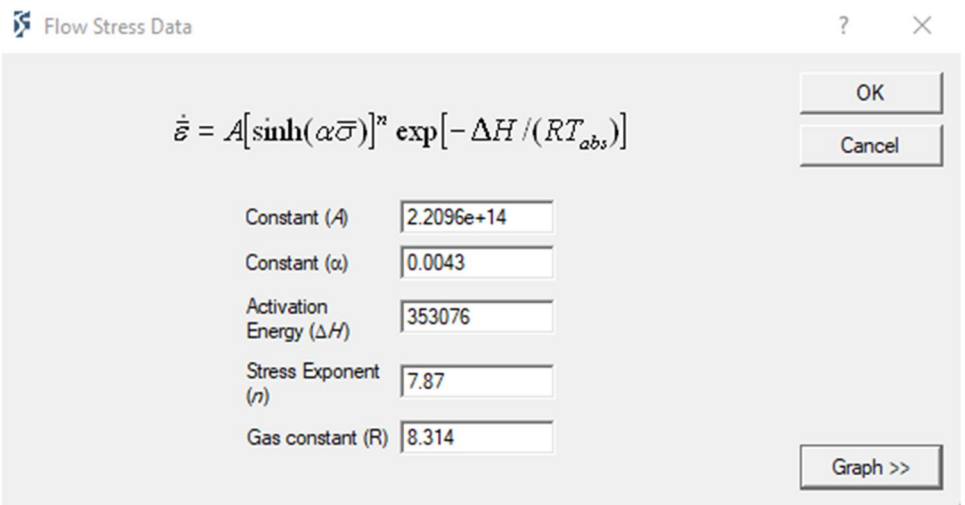

Fig. 9 Flow stress data (showing development of material database)

Table 5 Numerical simulation parameters

No	Description	Value
1	Workpiece material	AISI316 steel
2	Workpiece height (mm)	15
3	Workpiece diameter (mm)	10
4	Strain rate (s^{-1})	0.1
5	Workpiece temperature (°C)	900
6	Initial die temperature (°C)	200
7	Coefficient of heat convention (*N*/(s.mm.°C))	0.02
8	Coefficient of heat transfer (*N*/(s.mm.°C))	5
9	Coefficient of friction (lubricated)	0.3
10	FEM elements	26,247
11	Element nodes	5352
12	Simulation environment (°C)	25
13	Friction type	Shear

zones. Figure 10 illustrates the deformation zones. These zones are as follows[43]:

- Region 1—This region occurs at the centre of the specimen during deformation and undergoes severe shear, which extends to the sample corners. The severely deformed region forms the centre of interest for studying the deformation behaviour.
- Region 2—is the dead metal zone (DMZ). This region occurs at the die-workpiece contact surface region, which experiences low strain during deformation.
- Region 3—This region forms at the outer lateral surface of the specimen. The deformed region has a drum-shaped geometry and experiences moderate strains. Region c experiences maximum tensile stresses during forming, which may act as a crack initiation site.

A study has shown that metal flow behaviour during forming is inhomogeneous [17, 47, 55]. The inhomogeneous behaviour can be due to the variation in the deformation temperature. The temperature variation can be due to the conversion of plastic work into heat or the high heat conduction rate between the die and the workpiece during forming [24]. The temperature change causes microstructure variation, hence affecting the mechanical properties.

5.2 Stress and strain distribution at 900/1050 °C and 15 s^{-1}

Figures 11 and 12 show the deformation behaviour results from FEM simulation during forming at loading conditions of 900/1050 °C and 15 s^{-1}. The results from the selected three points (P1, P2, and P3) from the deformed sample show inhomogeneous deformation behaviour. Figures 11 and 12a show the temperature distribution during forming. Point P2 had the highest temperature drop of ~53.23 °C (Fig. 11) and ~25.45 °C (Fig. 12). This temperature drop was due to the chilling effect between the die and the workpiece interface [56, 57]. Points P1 and P3 exhibited a slight increase in the deformation temperature. The temperature increase was 59.88 °C (P1) and 39.35 °C (P2). The temperature increase may be due to the internal heat generation caused by severe plastic deformation during forming. The heat transfer in these two regions is between the workpiece and the environment. The temperature drops need attention during forming to ensure a uniform deformation process.

Figures 11 and 12b, c show the stress and strain distribution during forming. The results show variation in stress and strain distribution with the deformation time. The effective flow stress increased rapidly during the initial deformation stage. This behaviour was due to the high rate of dislocation density generation, causing work hardening (WH) [58]. At deformation time ~0.05 s, the flow stress attained steady-state condition due to the balance between WH and dynamic softening [59]. Points P1 and

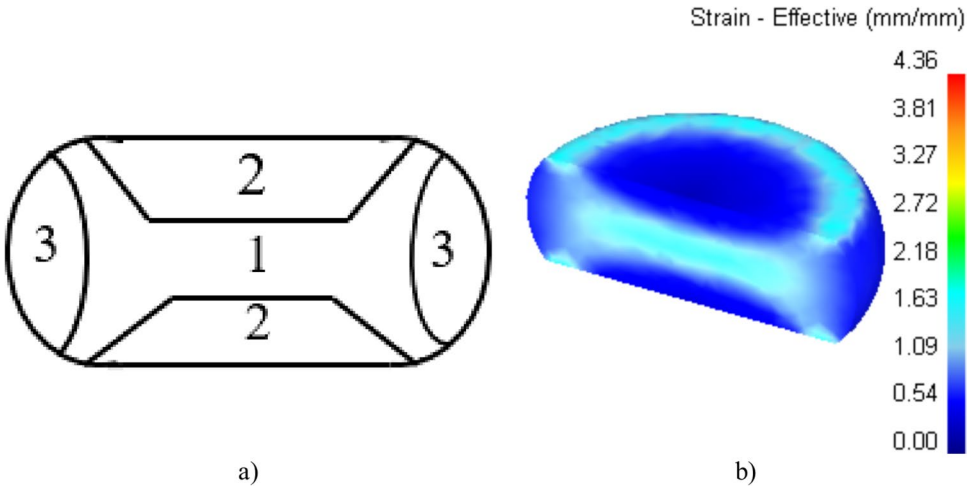

Fig. 10 Plots of deformation zones: **a** illustration of sample deformed zones and **b** strain distribution of deformed sample at $T = 1050$ °C and $\dot{\varepsilon} = 15\ s^{-1}$ (the colour code in the deformed sample indicate deformation zones)

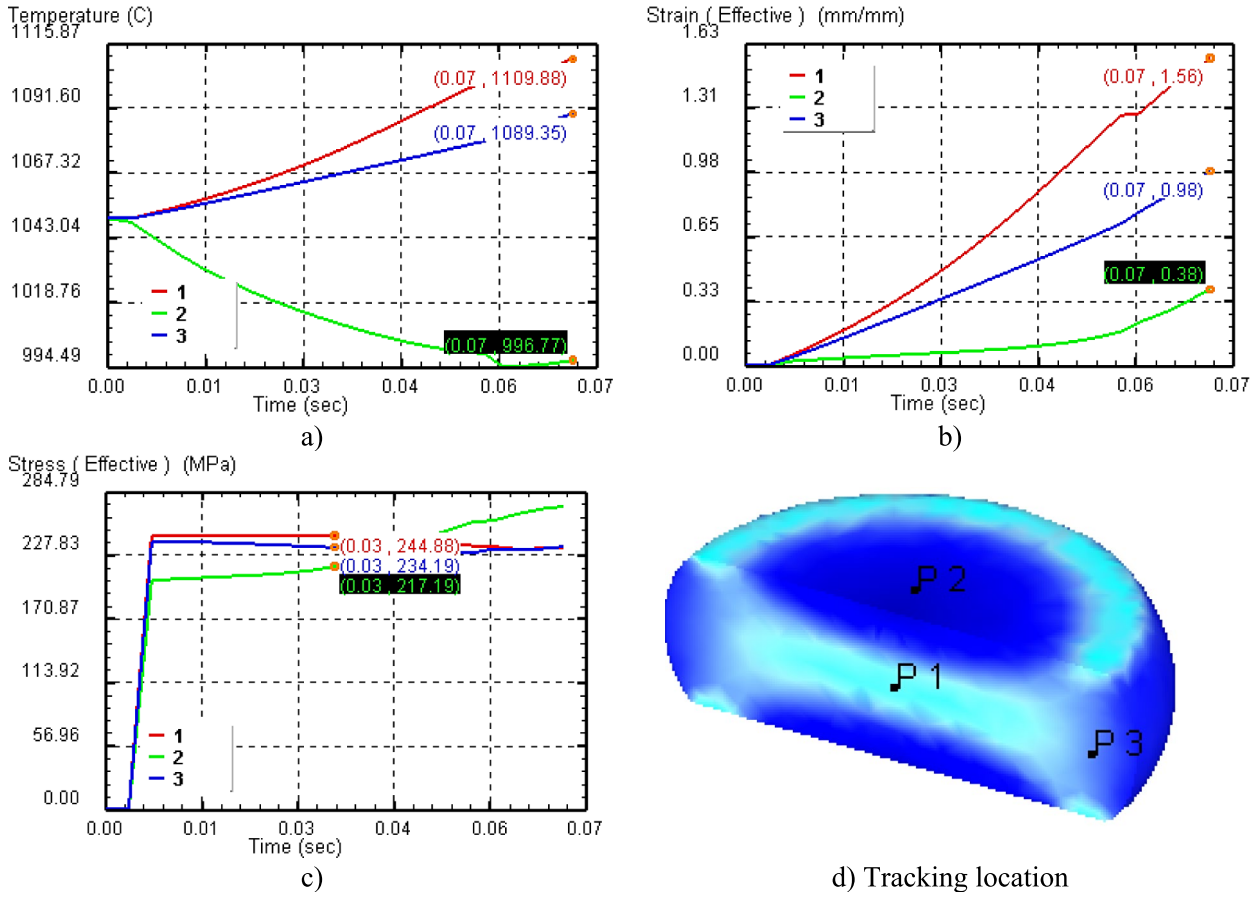

Fig. 11 Deformation behaviour at $T = 1050$ °C and $\dot{\varepsilon} = 15\ s^{-1}$ (the colour lines show the point tracking at different zones)

P3 had similar effective flow stress. These two points (P1 and P2) experienced relatively the same deformation temperature with no material restriction during deformation. Hence, there was less resistance to deformation. Point P2 had the highest effective stress due to metal restriction and chilling effect at the die−workpiece interface. Therefore, there is a need to optimise the temperature. Strain distribution was similar to that observed in stress distribution. Considering the point selected for analysis, point P2 had the lowest strain value. The lower strain value may be due to the frictional forces acting towards the sample centre, causing metal flow restriction at the sample surface. Point P1 had the highest strain value. This region (P1) experiences severe shearing due to large deformation forces. Grain refinement occurs in this region due to dynamic softening [56]. Point P3 exhibited moderate strain values less than P1 but higher than P2. The results show that the deformation was inhomogeneous. The prediction of a safe processing window for these loading conditions (900/1050 °C and 15 s^{-1}) needs further analysis.

5.3 Stress and strain distribution at 900/925 °C and 1 s^{-1}

Figures 12 and 13 show the stress, strain, and temperature distribution at 900/925 °C and 1 s^{-1} results from FEM simulation. This deformation region was identified as the 'safe' processing window from the processing map (Fig. 8). This region had a power dissipation efficiency of 27.5–34.0% and an instability value range of ~0.16–0.22. However, the temperature distribution graph indicates that in this deformation region, there was a temperature drop (Figs. 13 and 14). The temperature drop was: ~44.25% (900 °C/1 s^{-1}) and ~47.30% (925 °C/1 s^{-1}). The results indicate that after 4.20 s, the deformation occurred within the warm deformation zone. Hence, the deformation becomes difficult. Under these conditions, defects such as flow localisation and wedge cracking might occur. Therefore, these deformation conditions are not suitable for forming the studied steel. The FEM has accurately identified this region as the instability region.

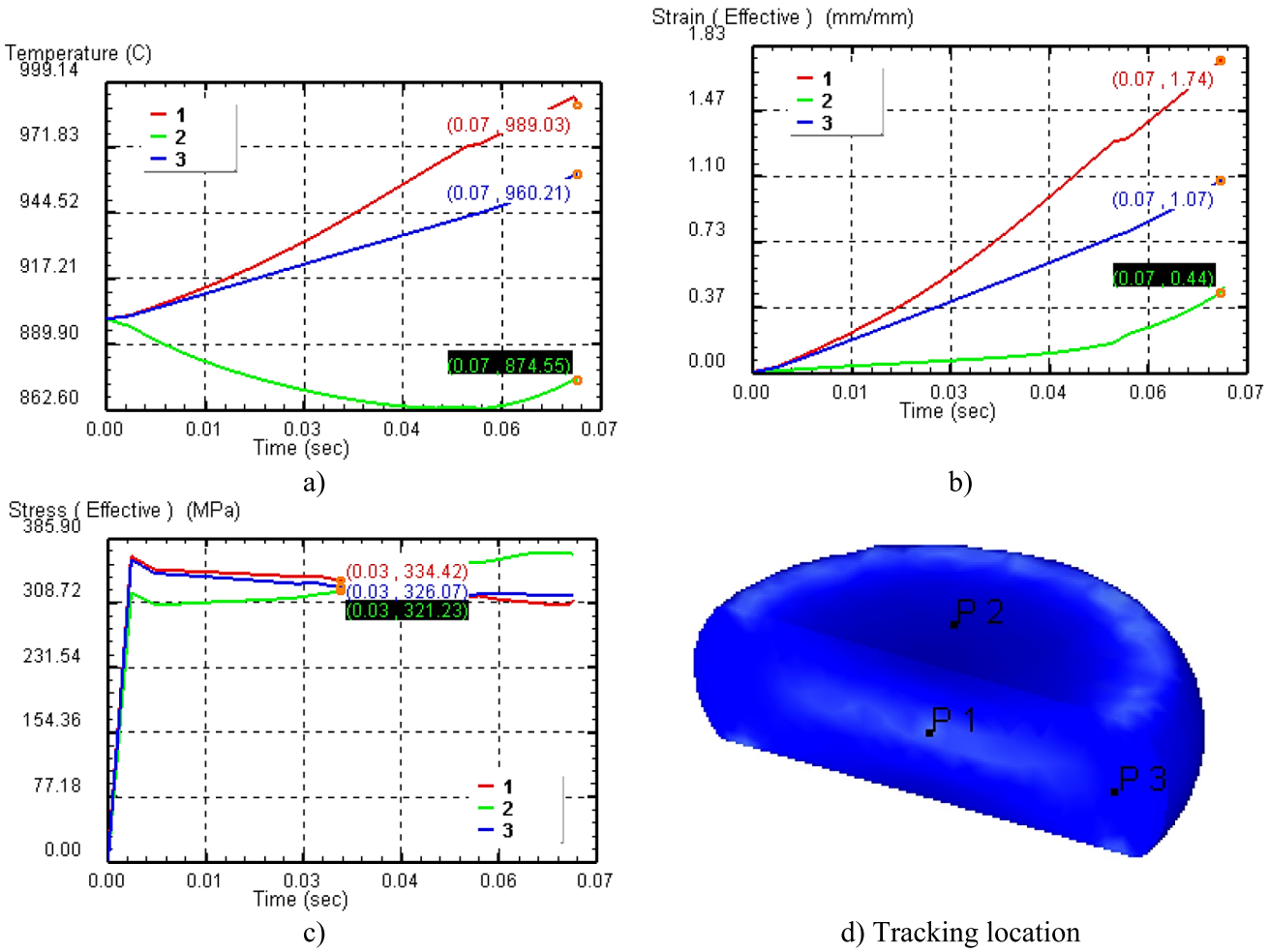

Fig. 12 Deformation behaviour at $T = 900$ °C and $\dot{\varepsilon} = 15\ s^{-1}$ (the colour lines show the point tracking at different zones)

The stress and strain distribution shows inhomogeneous deformation for the two deformation conditions (900/925 °C and 1 s^{-1}). Point P2 had the lowest strain value of 0.28 (900 °C and 1 s^{-1}) and 0.34 (925 °C and 1 s^{-1}), which may be due to interfacial friction between the die and the workpiece. The other points had a maximum strain value of 1.69 (P1) and 0.94 (P3) for 900 and 1 s^{-1} and 2.02 (P1) and 0.95 (P3) for 925 °C and 1 s^{-1}. The stress distribution curves of the three points show that the initial deformation increased rapidly up to 1.0 s. At this stage, work hardening dominated the deformation mechanism due to the high rate of dislocation density. After a deformation time of 1.0 s, the effective stress attained a steady-state condition for one second due to dynamic softening. At higher deformation times (≥ 2.0 s), the effective stress increased with an increase in the deformation time (Figs. 13 and 14c). At this stage, the effective stress exhibited work-hardening flow characteristics. Under these forming conditions (900/925 °C and 1 s^{-1}), WH controlled the deformation process. Hence, the loading conditions were unsuitable for the deformation of the steel studied. The FEM simulation results have shown that processing maps are not sufficient to determine the optimal processing window for improved product quality. Therefore, to avoid experimental costs and time, the authors of this article suggest coupling FEM simulations and processing maps in determining the optimal processing parameters for the metal forming processes.

6 Conclusion

In this study, uniaxial compression tests were conducted using the Gleeble® equipment. The loading conditions were 900–1050 °C and 0.1–15 s^{-1}. The experimental data were used to develop constitutive equations and processing

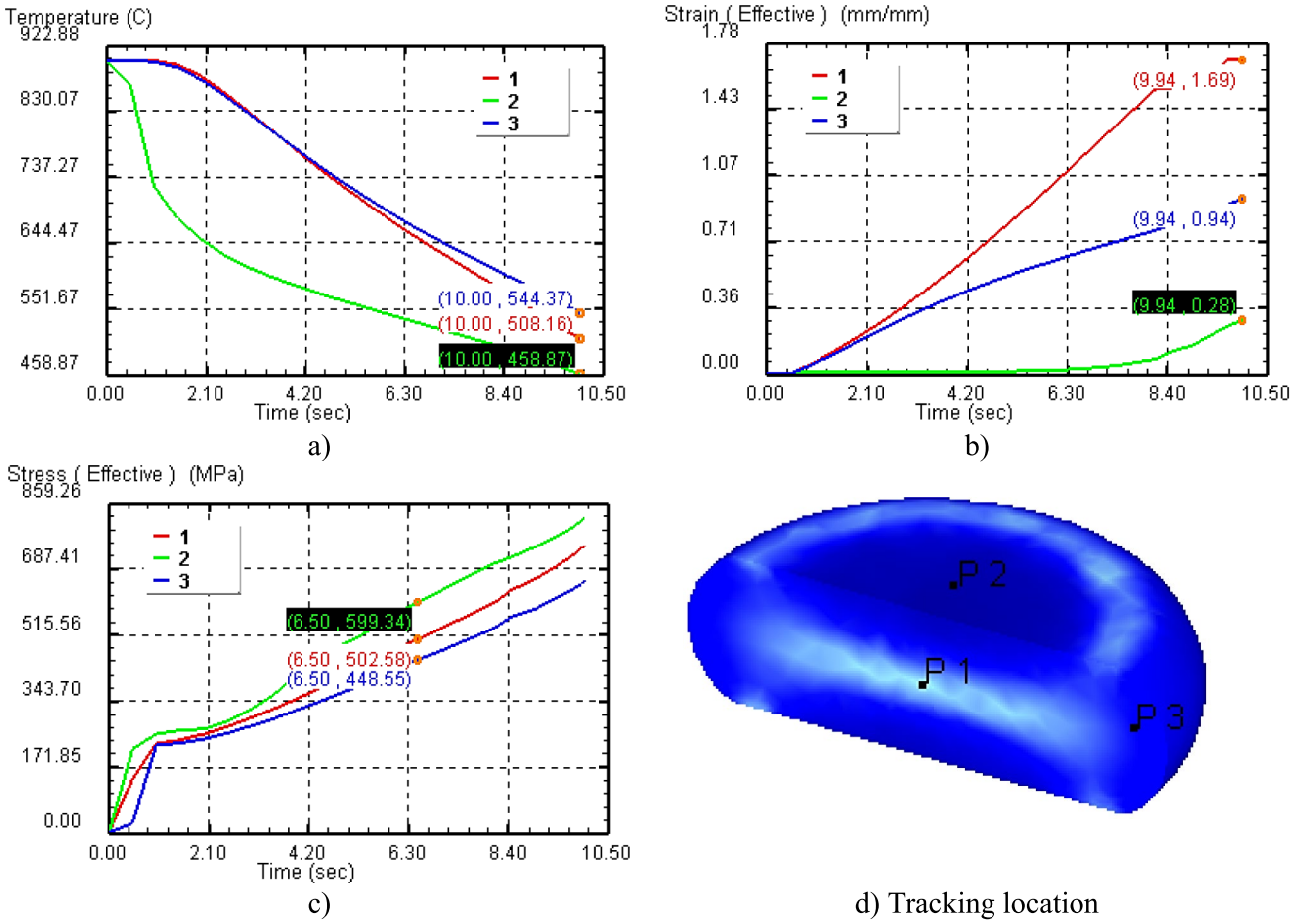

Fig. 13 Deformation behaviour at $T = 900$ °C and $\dot{\varepsilon} = 1\ s^{-1}$ (the colour lines show the point tracking at different zones)

maps. The identified optimal processing window using processing maps were verified by FEM simulation. From the study, the conclusions were as follows:

1. The flow stress–strain curves show that the deformation process is sensitive to the loading conditions (temperature, strain rate, and strain). At a given temperature, the flow stress increased as the strain rate increased and vice versa. During the initial deformation stage (< 0.2 strain), the flow stress–strain curves exhibited work-hardening behaviour. This flow behaviour indicates that WH controlled the deformation process. At higher strain (> 0.2), the flow stress–strain curve exhibited steady-state flow stress. This characteristic behaviour indicates that dynamic recovery DRV controlled the deformation process.
2. Using the Arrhenius equation, the obtained material parameters were stress exponent (7.87) and activation energy (353.076 kJ mol^{-1}). The constitutive equation developed for the studied steel is as follows:

$$\dot{\varepsilon} = 2.2096 \times 10^{14} sinh(0.0043\sigma_{ss})^{7.87} exp\left[\frac{-353076}{RT}\right]$$

$$\sigma_{ss} = \frac{1}{0.0043} In\left[\left(\frac{Z}{2.2096 \times 10^{14}}\right)^{\frac{1}{8}} + \left(\left(\frac{Z}{2.2096 \times 10^{14}}\right)^{\frac{2}{7.87}} + 1\right)^{\frac{1}{2}}\right]$$

$$Z = \dot{\varepsilon}\left[\frac{353076}{RT}\right] = 2.2096 \times 10^{14}\left(sinh(0.0043\sigma_{ss}\right)^{7.87}$$

3. A comparison between experimental and predicted data using the developed constitutive equation was analysed using statistical parameters. The statistical parameter values were Pearson's coefficient R (0.995) and average absolute relative error (2.53%). The statistical parameters show a good correlation between the predicted

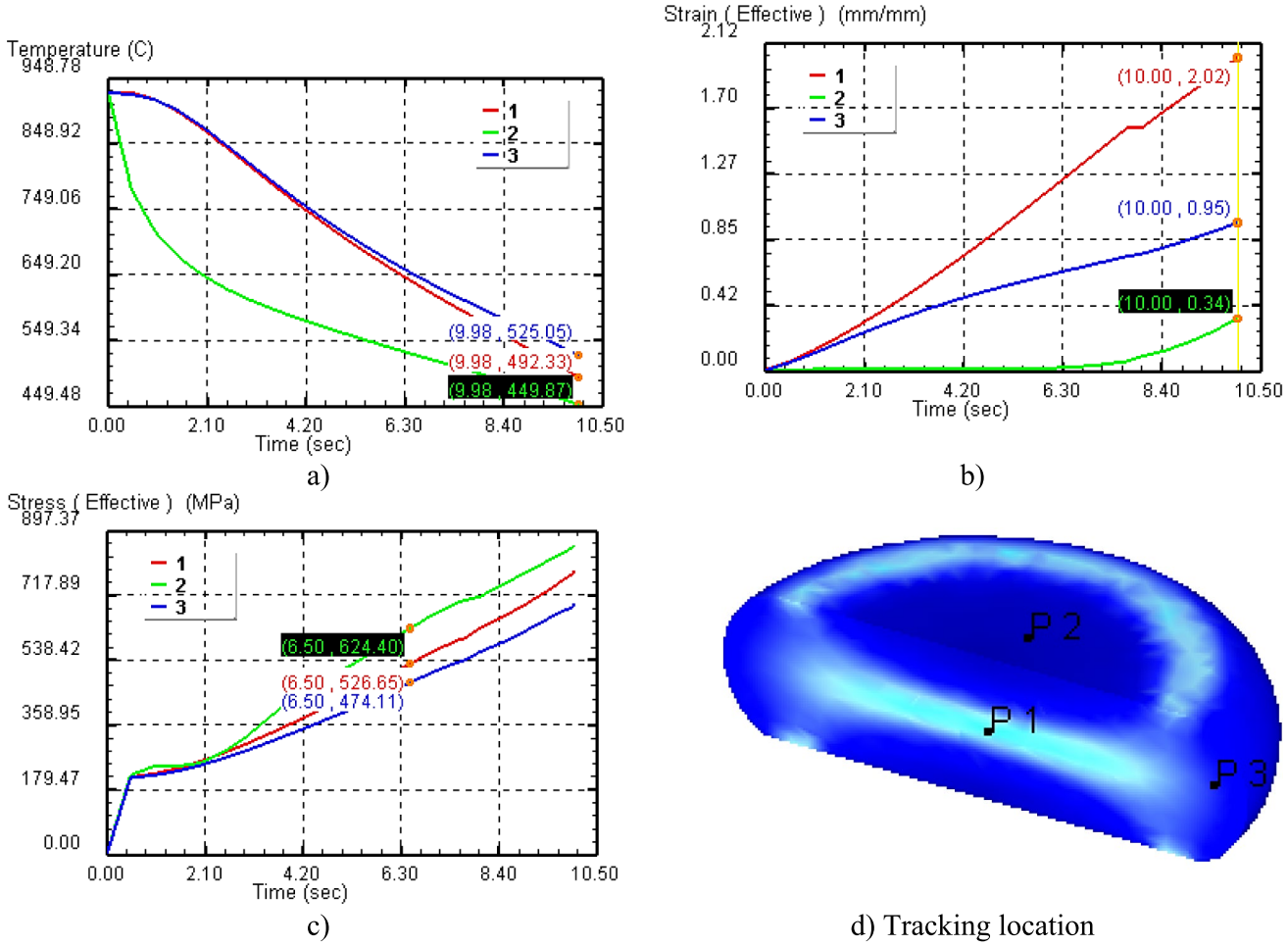

Fig. 14 Deformation behaviour at $T = 925$ °C and $\dot{\varepsilon} = 1\ s^{-1}$ (the colour lines show the point tracking at different zones)

and experimental data. Hence, the developed constitutive model has higher accuracy. This model can predict the flow stress behaviour of the steel studied.

4. The optimal processing window was identified using processing maps. Two 'safe' or 'stable' regions were identified:
   - 900–925 °C and 1 s^{-1} with η-value of 27.5–34%
   - 900/1050 °C and 15 s^{-1} with η-value of 24–27%
5. The FEM simulation was conducted using the optimal processing conditions. From simulation analysis, the optimal processing conditions were 900/1050 °C and 15 s^{-1}. The FEM simulation provides a more accurate prediction of the optimal processing condition.

Author contribution All authors contributed to the conceptualisation and research design. The research methodology and investigations were performed by Japheth Obiko, Micheal Bodunrin, Desmond Klenam, Brendon Mxolisi, and Malatji Nicholus. The first draft of the manuscript was written by Japheth Obiko, and all authors commented on previous versions of the manuscript. All authors read and approved the final manuscript.

Funding Open access funding provided by Tshwane University of Technology.

Declarations

Competing interests The authors declare no competing interests.

Open Access This article is licensed under a Creative Commons Attribution 4.0 International License, which permits use, sharing, adaptation, distribution and reproduction in any medium or format, as long as you give appropriate credit to the original author(s) and the source, provide a link to the Creative Commons licence, and indicate if changes were made. The images or other third party material in this article are included in the article's Creative Commons licence, unless indicated otherwise in a credit line to the material. If material is not included in the article's Creative Commons licence and your intended use is not permitted by statutory regulation or exceeds the permitted use, you will need to obtain permission directly from the copyright holder. To view a copy of this licence, visit http://creativecommons.org/licenses/by/4.0/.

References

1. Kotkunde N, Krishnamurthy HN, Singh SK, Jella G (2018) Experimental and numerical investigations on hot deformation behavior and processing maps for ASS 304 and ASS 316. High Temp Mater Process 37(9–10):873–888. https://doi.org/10.1515/htmp-2017-0047
2. Wenhui Z, Shuhua S, Deli Z, Baozhong W, Zhenhua W, Wantang F (2011) Hot deformation behavior of a Nb-containing 316LN stainless steel. Mater Des 32(8–9):4173–4179. https://doi.org/10.1016/j.matdes.2011.04.043
3. Ferreira RP, Nascimento CCF, Reis GS, Silva ES, Rodrigues SF (2020) Thermomechanical behavior and corrosion resistance of a 316 L austenitic stainless steel. Mater Sci Appl 11(04):217–233. https://doi.org/10.4236/msa.2020.114015
4. Han Y, Zou D, Chen Z, Fan G, Zhang W (2011) Investigation on hot deformation behavior of 00Cr23Ni4N duplex stainless steel under medium-high strain rates. Mater Charact 62(2):198–203. https://doi.org/10.1016/j.matchar.2010.11.013
5. Wang LJ, Sheng LY, Hong CM (2012) Influence of grain boundary carbides on mechanical properties of high nitrogen austenitic stainless steel. Mater Des 37:349–355. https://doi.org/10.1016/j.matdes.2012.01.024
6. Türkmen M, Tanouz AM, Akgün M, Erden MA (2023) The effect of Mn and Ti ratio on microstructure and mechanical and machinability properties of 316 L stainless steel used in biomedical applications. Metals (Basel) 13(11):pp. https://doi.org/10.3390/met13111804
7. Zhang X, Xiao Y, Cai Y (2024) Effect of Ni element on microstructure and properties of cold-rolled 316 L austenitic stainless steel. Mater Res Express 11(3):pp. https://doi.org/10.1088/2053-1591/ad2f79
8. Lee WS, Chen TH, Lin CF, Luo WZ (2011) Dynamic mechanical response of biomedical 316L stainless steel as function of strain rate and temperature. Bioinorg Chem Appl 2011:1. https://doi.org/10.1155/2011/173782
9. Kruml T, Polák J, Degallaix S (2000) Microstructure in 316LN stainless steel fatigued at low temperature. Mater Sci Eng A 293(1–2):275–280. https://doi.org/10.1016/S0921-5093(00)01015-7
10. Silva G, Baldissera MR, De Sousa Trichês E, Cardoso KR (2013) Preparation and characterization of stainless steel 316L/HA biocomposite. Mater Res 16(2):304–309. https://doi.org/10.1590/S1516-14392012005000182
11. Alhazaa A, Haneklaus N (2020) Diffusion bonding and Transient Liquid Phase (TLP) bonding of type 304 and 316 austenitic stainless steel—a review of similar and dissimilar material joints. Metals (Basel) 10(5):pp. https://doi.org/10.3390/met10050613
12. Chen L, Luo R, Yang Y, Peng C, Gui X, Zhang J, Song K, Gao P, Cheng X (2019) Investigation on the hot deformation behavior of 316L stainless steel using 3D processing map. Trans Indian Inst Met 72(12):2997–3006. https://doi.org/10.1007/s12666-019-01674-4
13. Hong CM, Shi J, Sheng LY, Cao WC, Hui WJ, Dong H (2011) Effects of hot-working parameters on microstructural evolution of high nitrogen austenitic stainless steel. Mater Des 32(7):3711–3717. https://doi.org/10.1016/j.matdes.2011.03.055
14. Marchattiwar A, Sarkar A, Chakravartty JK, Kashyap BP (2013) Dynamic recrystallization during hot deformation of 304 austenitic stainless steel. J Mater Eng Perform 22(8):2168–2175. https://doi.org/10.1007/s11665-013-0496-0
15. Ouyang W, Li Z, Haichen W, Di W, Shuowen Z, Xiu Q, Shilong J, Shujun L, Wenwu Z, Liyuan S (2024) Optimized mechanical properties of the hot forged Ti–6Al–4V alloy by regulating multiscale microstructure via laser shock peening. Int J Mach Tools Manuf 201(July). https://doi.org/10.1016/j.ijmachtools.2024.104192
16. Gao F, Liu W, Zhu Q, Gao Z, Misra K, Liu Z, Yu F (2020) Flow behaviour and constitutive modeling for hot deformation of austenitic stainless steel. Mater Res Express 7(11):116512. https://doi.org/10.1088/2053-1591/abb151
17. Obiko JO, Mwema FM, Bodunrin MO (2019) Finite element simulation of X20CrMoV121 steel billet forging process using the deform 3D software. SN Appl Sci 1(9):1–10. https://doi.org/10.1007/s42452-019-1087-y
18. Fangpo L, Ning L, Xiaojian R, Song Q, Caihong L, Jianjun W, Bin W (2023) Arrhenius constitutive equation and artificial neural network model of flow stress in hot deformation of offshore steel with high strength and toughness. Mater. Technol. 38(1):pp. https://doi.org/10.1080/10667857.2023.2264670
19. Li N, Zhao C, Jiang Z, Zhang H (2019) Flow behavior and processing maps of high-strength low-alloy steel during hot compression. Mater Charact 153(2018):224–233. https://doi.org/10.1016/j.matchar.2019.05.009
20. Sanrutsadakorn A, Uthaisangsuk V, Suranuntchai S, Thossatheppitak B (2013) Investigation of hot deformation characteristics of AISI 4340 steel using processing map. Adv Mater Res 683:301–306. https://doi.org/10.4028/www.scientific.net/AMR.683.301
21. Park J, Kim Y, Shin S, Kim N (2022) Characterization of hot workability in AISI 4340 based on a 3D processing map. Metals (Basel) 12(11):pp. https://doi.org/10.3390/met12111946
22. Łukaszek-Sołek A, Krawczyk J, Śleboda T, Grelowski J (2019) Optimization of the hot forging parameters for 4340 steel by processing maps. J Mater Res Technol 8(3):3281–3290. https://doi.org/10.1016/j.jmrt.2019.05.018
23. Jeong HY, Park J, Kim Y, Shin SY, Kim N (2023) Processing parameters optimization in hot forging of AISI 4340 steel using instability map and reinforcement learning. J Mater Res Technol 23:1995–2009. https://doi.org/10.1016/j.jmrt.2023.01.106
24. Evans RW, Scharning PJ (2001) Axisymmetric compression test and hot working properties of alloys. Mater Sci Technol 17(8):995–1004. https://doi.org/10.1179/026708301101510843
25. Shi RX, Liu ZD (2011) Hot deformation behavior of P92 steel used for ultra-super-critical power plants. J Iron Steel Res Int 18(7):53–58. https://doi.org/10.1016/S1006-706X(11)60090-3
26. Fang XQ, Bin Wang J, Liu SY, Wen JZ, Song HY, Liu HT (2024) Microstructure evolution, hot deformation behavior and processing maps of an FeCrAl alloy. Materials (Basel) 17(8):1847. https://doi.org/10.3390/ma17081847
27. Zhou X, Ma W, Feng C, Zhang L (2020) Flow stress modeling, processing maps and microstructure evolution of 05Cr17Ni4Cu4Nb martensitic stainless steel during hot plastic deformation. Mater Res Express 7(4):pp. https://doi.org/10.1088/2053-1591/ab89d8
28. Zhu L (2018) A two-stage constitutive model of X12CrMoWVNbN10-1-1 steel during elevated temperature. Mater Res Express 5:1–11
29. Rastegari H, Kermanpur A, Najafizadeh A, Porter D, Somani M (2015) Warm deformation processing maps for the plain eutectoid steels. J Alloys Compd 626:136–144. https://doi.org/10.1016/j.jallcom.2014.11.170
30. Liu CY, Zhang RJ, Yan YN (2011) Hot deformation behaviour and constitutive modelling of P92 heat resistant steel. Mater Sci Technol 27(8):1281–1286. https://doi.org/10.1179/026708310x12683158443323
31. Sellars CM, McTegart WJ (1966) On the mechanism of hot deformation. Acta Metall 14(9):1136–1138. https://doi.org/10.1016/0001-6160(66)90207-0
32. Ji H, Cai Z, Pei W, Huang X, Lu Y (2020) DRX behavior and microstructure evolution of 33Cr23Ni8Mn3N: experiment and finite element simulation. J Mater Res Technol 9(3):4340–4355. https://doi.org/10.1016/j.jmrt.2020.02.059

33. Xiao X, Liu Q, Hu F, Zheng X, Wang N, Chen J, Ullah A (2012) A comparative study on Arrhenius-type constitutive equations and artificial neural network model to predict high-temperature deformation behaviour in 12Cr3WV steel. Comput Mater Sci 62:227–234. https://doi.org/10.1016/j.commatsci.2012.05.053
34. Zhang G, Zhou Z, Sun H, Zou L, Wang M, Li S (2014) Hot deformation behavior and processing map of a 9Cr ferritic/martensitic ODS steel. J Nucl Mater 455(1–3):139–144. https://doi.org/10.1016/j.jnucmat.2014.05.043
35. Laasraoui A, Jonas JJ (1991) Prediction of steel flow stresses at high temperatures and strain rates. Metall Trans A 22(7):1545–1558. https://doi.org/10.1007/BF02667368
36. Menapace C, Sartori N, Pellizzari M, Straffelini G (2018) Hot deformation behavior of four steels: a comparative study. J Eng Mater Technol Trans ASME 140(2):021006. https://doi.org/10.1115/1.4038670
37. Carsí M, Peñalba F, Rieiro I, Ruano OA (2011) High temperature workability behavior of a modified P92 steel. Int J Mater Res 102(11):1378–1383. https://doi.org/10.3139/146.110603
38. Niu X, Shen L, Chen C, Zhou J, Chen L (2019) An Arrhenius - type constitutive model to predict the deformation behavior of Sn0. 3Ag0. 7Cu under different temperature. J Mater Sci Mater Electron 2(0123456789):pp. https://doi.org/10.1007/s10854-019-01833-9
39. Nayan N, Singh G, Souza PM, Murty SN, Venkatesh M, Shivram BR, Narayanan PR, Mohan M, Jha SK (2021) Hot workability and microstructure control in Monel®400 (Ni–30Cu) alloy: an approach using processing map, constitutive equation and deformation modeling. Mater Sci Eng A825(July):141855. https://doi.org/10.1016/j.msea.2021.141855
40. Prasad YVRK, Rao KP, Sasidhara S (2015) Hot working guide a compendium of processing maps. https://doi.org/10.1016/B978-0-08-033454-7.50019-X
41. Kishor B, Chaudhari GP, Nath SK (2016) Hot deformation characteristics of 13Cr-4Ni stainless steel using constitutive equation and processing map. J Mater Eng Perform 25(7):2651–2660. https://doi.org/10.1007/s11665-016-2159-4
42. Narayana Murty SVS, Nageswara Rao B (1998) Ziegler's criterion on the instability regions in processing maps. J. Mater. Sci. Lett. 17(14):1203–1205. https://doi.org/10.1023/A:1006541710533
43. Obiko J, Chown L, Whitefield D, Bodunrin M (2022) Understanding hot workability of power plant P92 creep resistant steels using dynamic material modelling (DMM) and microstructural evolution. Int J Interact Des Manuf. https://doi.org/10.1007/s12008-022-01084-9
44. Narayana Murty SVS, Nageswara Rao B, Kashyap BP (2000) Instability criteria for hot deformation of materials. Int. Mater. Rev. 45(1):15–26. https://doi.org/10.1179/095066000771048782
45. Ma X, Zeng W, Sun Y, Zhao Y, Wang S, Zhou Y (2010) A comparative study of various flow instability criteria in processing map. Xiyou Jinshu Cailiao Yu Gongcheng/Rare Met Mater Eng 39(5):756–761. https://doi.org/10.1016/s1875-5372(10)60096-3
46. Wu H, Liu M, Wang Y, Huang Z, Tan G, Yang L (2020) Experimental study and numerical simulation of dynamic recrystallization for a FGH96 superalloy during isothermal compression. J Mater Res Technol 9(3):5090–5104. https://doi.org/10.1016/j.jmrt.2020.03.026
47. Rahul MR, Samal S, Venugopal S, Phanikumar G (2018) Experimental and finite element simulation studies on hot deformation behaviour of AlCoCrFeNi2.1 eutectic high entropy alloy. J Alloys Compd 749:1115–1127. https://doi.org/10.1016/j.jallcom.2018.03.262
48. Lin YC, Chen MS, Zhong J (2008) Numerical simulation for stress/strain distribution and microstructural evolution in 42CrMo steel during hot upsetting process. Comput Mater Sci 43(4):1117–1122. https://doi.org/10.1016/j.commatsci.2008.03.010
49. Ji X, Tian Q, Tan Y, Huang C, Wan M, Li R (2023) Simulation and experimental study of hot deformation behavior in near β phase region for TC21 alloy with a forged structure. Crystals 13(10):pp. https://doi.org/10.3390/cryst13101524
50. Maarefdoust M, Hosseyni M (2011) Simulation and analysis of finite volume of hot forging process of nut. in AIP Conference Proceedings 1383(1):581–587. https://doi.org/10.1063/1.3623660
51. Obiko J, Shongwe MB, Malatji N (2024) On the effect of deformation conditions on the metal flow behavior during upsetting process using finite element simulation DEFORM 3D software. Int J Interact Des Manuf. https://doi.org/10.1007/s12008-024-02051-2
52. Obiko J, Shongwe B, Malatji N, Bodunrin M, Klenam D (2024) Effect of aspect ratio on the metal flow behaviour during forming process: a numerical simulation approach. Sci African 25(May):e02265. https://doi.org/10.1016/j.sciaf.2024.e02265
53. Efa DA, Lemu HG, Gutema EM, Gopal M (2024) Analyzing the effect of temperature on alloy steel forging simulation using finite element simulation. Key Eng Mater 979:81–92. https://doi.org/10.4028/p-a6inh6
54. Lv C, Zhang L, Mu Z, Tai Q, Zheng Q (2008) 3D FEM simulation of the multi-stage forging process of a gas turbine compressor blade. J Mater Process Technol 198(1–3):463–470. https://doi.org/10.1016/j.jmatprotec.2007.07.032
55. Li YP, Onodera E, Matsumoto H, Chiba A (2009) Correcting the stress-strain curve in hot compression process to high strain level. Metall. Mater. Trans. A Phys. Metall. Mater. Sci. 40(4):982–990. https://doi.org/10.1007/s11661-009-9783-7
56. Rasti J, Najafizadeh A, Meratian M (2011) Correcting the stress-strain curve in hot compression test using finite element analysis and Taguchi method. Int J ISSI 8(1):26–33
57. Obiko J, Mwema F (2020) Deformation behaviour of high-strength aluminium alloy during forging process using finite element method. Eng Solid Mech 9(1):31–40. https://doi.org/10.5267/j.esm.2020.6.001
58. Zhu L, He J, Zhang Y (2018) A two-stage constitutive model of X12CrMoWVNbN10–1–1 steel during elevated temperature. Mater. Res. Express 5(2):pp. https://doi.org/10.1088/2053-1591/aaa911
59. Cai Z, Ji H, Pei W, Wang B, Huang X, Li Y (2019) Constitutive equation and model validation for 33Cr23Ni8Mn3N heat-resistant steel during hot compression. Results Phys 15(July):102633. https://doi.org/10.1016/j.rinp.2019.102633

Publisher's Note Springer Nature remains neutral with regard to jurisdictional claims in published maps and institutional affiliations.